JOURNAL OF COMPUTATIONAL PHYSICS 115, 184–199 (1994)

Multidomain Spectral Solution of Compressible Viscous Flows

DAVID A. KOPRIVA

Supercomputer Computations Research Institute, B-186, Florida State University, Tallahassee, Florida 32306

Received February 16, 1993; revised September 7, 1993

We develop a nonoverlapping multidomain spectral collocation method to solve compressible viscous flows. At the interfaces, the advection terms are treated with a characteristic correction method. The diffusion terms are treated with a penalty method. Spectral accuracy is demonstrated on linear model problems in one and two space dimensions. The method is applied to a subsonic and a supersonic flow over a flat plate. The results are compared to solutions of the boundary-layer equations which show that two digit accuracy in the adiabatic plate temperature is obtained with 16 points in the boundary layer for a freestream Mach number of two. A second application is to a transonic flow in a two-dimensional converging-diverging nozzle, where the computed results are compared to experimental data.

1. INTRODUCTION

In this paper we present a nonoverlapping spectral collocation domain decomposition method to compute steady solutions of the compressible Navier–Stokes equations. These solutions typically have multiple length scales that might be associated with the size of an aerodynamic body, the distance between shock waves, the size of entropy and vorticity layers, and the size of viscous boundary layers. Such flows would be difficult to treat with a standard spectral method. By varying the size and resolution of the subdomains, a multidomain method can be used to resolve efficiently multiple length scales with fewer grid points than a single domain method might require.

Domain decomposition techniques have become very important tools for the application of spectral collocation methods. A review of several techniques can be found in the book by Canuto *et al.* [1]. In addition to the ability to resolve flows without complicated mappings, the conditioning of the individual subproblems is significantly better. It is cheaper to compute solutions for a given number of points by breaking up the problem into several subproblems, since the work required by a spectral method varies nonlinearly with the number of grid points. For time dependent problems, or problems where a pseudo-time is used to converge to a steady state, larger time steps can be used. This is because the size of the time step depends more strongly on the number of modes used in the approximation ($O(N^2)$ or $O(N^4)$ for first or second derivative problems in one space dimension), than on the size of the domain. Finally, roundoff errors are less likely to be a problem when smaller grid sizes are used.

The design of spectral domain decomposition algorithms has emphasized the solution of incompressible viscous flows. Representative examples of such methods include the spectral element method [2], the pseudospectral matrix element method [3], and the flux conservation method [4]. In these papers applications have been made to a variety of fluid flows in both two and three space dimensions.

For compressible flows, the emphasis has been on the solution of the inviscid Euler equations. Methods for these equations have been presented in [5–7]. Applications include the solution of the blunt body problem, e.g., [8, 9], and the interaction of shock waves with free-stream disturbances [10, 11]. For viscous compressible flows, the global flux conservation method has been used in [4] to solve a one-dimensional nonequilibrium shock flow.

The difference between the method described here and that of [4] is in the way that the interfaces are treated. We use an upwind characteristic method for the advection terms that is identical to the method for the Euler equations [5]. Thus, as the viscosity goes to zero, the inviscid algorithm is recovered. Next, a penalty method is used to treat the viscous terms at an interface. A weighted average of the viscous terms is computed at each interface point. A penalty that is proportional to the jump in the viscous fluxes is applied to the result to produce a stable approximation. Methods of this type have been used for the solution of the Poisson equation [12] and for the incompressible Navier Stokes equations [13]. We base our treatment of the viscous terms on the ideas presented in [14, 15]. In [14], stability was proved for a particular choice of the weighting and penalty coefficients, and the method was shown to be equivalent to a variational method when applied to the Poisson equation. The Chebyshev approximation was considered in [15]. The computational

0021-9991/94 $6.00

advantages of this interface technique is that it is applied pointwise; it is not restricted to Laplace-type operators; and it can be naturally extended to three-dimensional geometries. Finally, it is also not tied to any particular time differencing scheme.

We begin the description of the algorithm in Section 3. We solve the advection–diffusion equation, Burger's equation, and a quasi-one-dimensional viscous flow in a converging–diverging nozzle, all in one space dimension. Next, we describe the interface method in two dimensions. Finally, in Section 4 we use the method to compute a subsonic and a supersonic flow over a flat plate and transonic flow in a converging–diverging nozzle. The boundary layer results are compared to compressible boundary layer solutions. The nozzle solution is compared to experimental data.

2. THE VISCOUS COMPRESSIBLE FLOW EQUATIONS

We seek the solution of the compressible Navier–Stokes equations in the nonconservative form

$$\begin{aligned}
&\rho_t + u\rho_x + v\rho_y + \rho u_x + \rho v_y = 0\\
&u_t + uu_x + vu_y + \frac{p_x}{\rho} = \frac{\sqrt{\gamma}\, M_{\text{ref}}}{\rho\, \text{Re}}\,\tau^x\\
&v_t + uv_x + vv_y + \frac{p_y}{\rho} = \frac{\sqrt{\gamma}\, M_{\text{ref}}}{\rho\, \text{Re}}\,\tau^y\\
&p_t + up_x + vp_y + \gamma p \nabla\cdot\mathbf{q}\\
&\qquad = \frac{\gamma\sqrt{\gamma}\, M_{\text{ref}}}{\text{Pr Re}}\nabla\cdot(\kappa\nabla T) + \frac{(\gamma-1)\sqrt{\gamma}\, M_{\text{ref}}}{\text{Re}}\,\Phi,
\end{aligned} \tag{1}$$

where

$$\begin{aligned}
\tau^x &= \frac{\partial}{\partial x}(\mu(4u_x - 2v_y)/3) + \frac{\partial}{\partial y}(\mu(v_x + u_y))\\
\tau^y &= \frac{\partial}{\partial x}(\mu(v_x + u_y)) + \frac{\partial}{\partial y}(\mu(4v_y - 2u_x)/3)\\
\Phi &= \frac{\mu u_x}{3}(4u_x - 2v_y) + \mu(u_y + v_x)^2 + \frac{\mu v_y}{3}(4v_y - 2u_x)
\end{aligned} \tag{2}$$

and the subscripts in (1) and (2) represent partial differentiation, e.g., $u_x = \partial u/\partial x$.

Although we are typically interested in the steady solution, it is most common to compute the steady solution of the compressible Navier–Stokes equations as the asymptotic long time solution of the unsteady equations. With minor modifications, the algorithm can be applied to the equations in conservative form as well.

In these equations, we have scaled the dimensional pressure, density, velocity, and temperature (p^*, ρ^*, $\mathbf{q}^*$, T^*) by

$$\begin{aligned}
p &= p^*/p_{\text{ref}}\\
\rho &= \rho^*/\rho_{\text{ref}}\\
\mathbf{q} &= (u, v) = \mathbf{q}^*/\sqrt{p_{\text{ref}}/\rho_{\text{ref}}}\\
T &= T^*\Big/\left(\frac{p_{\text{ref}}}{\mathbf{R}\rho_{\text{ref}}}\right),
\end{aligned} \tag{3a}$$

where $\mathbf{R}$ is the gas constant. We scale the dimensional space and time by

$$\begin{aligned}
\mathbf{x} &= \mathbf{x}^*/L\\
t &= t^*\sqrt{p_{\text{ref}}/\rho_{\text{ref}}}/L,
\end{aligned} \tag{3b}$$

where L represents the length scale.

The temperature is computed by the perfect gas equation of state, which becomes

$$T = p/\rho \tag{4}$$

under the scaling (3). The dimensionless variables in (1) are the standard Reynolds number (Re), which is scaled to the characteristic length, the Prandtl number (Pr), and the Mach number (M).

To compute the viscosity coefficient, we use the Sutherland law [16]

$$\mu = \frac{\mu^*}{\mu_{\text{ref}}} = \frac{1 + 198.6/T_{\text{ref}}}{T + 198.6/T_{\text{ref}}}\,T^{3/2} \tag{5}$$

where T_{ref} is measured in $^\circ R$. This formula is applicable within the range 180–3400 $^\circ R$. We assume that the Prandtl number is constant, so the same formula is used to compute the dimensionless heat conductivity, κ.

3. THE SPECTRAL MULTIDOMAIN ALGORITHM

3.1. Linear, One-Dimensional Problems

To motivate the interface condition for the viscous terms in the compressible Navier–Stokes equations, (1), we consider the two-domain collocation approximation to the diffusion equation

$$\begin{aligned}
&u_t = u_{xx}, \qquad x \in [a, c], \quad t > 0\\
&u(x, 0) = u_0(x)\\
&u(a, t) = u(c, t) = 0.
\end{aligned} \tag{6}$$

The interval $[a, c]$ is subdivided into two subintervals as shown in Fig. 1. The two-domain problem satisfies the equations

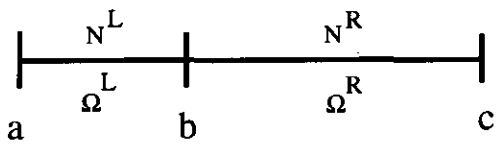

FIG. 1. Subdivision of the interval $[a, c]$.

$$\begin{aligned} u_t^L &= u_{xx}^L, \qquad x \in \Omega^L, \quad t > 0 \\ u^L(x, 0) &= u_0(x) \\ u^L(a, t) &= 0 \\ u_t^R &= u_{xx}^R, \qquad x \in \Omega^R, \quad t > 0 \\ u^R(x, 0) &= u_0(x) \\ u^R(c, t) &= 0. \end{aligned} \tag{7}$$

At the interface, $x = b$, the solution satisfies the continuity condition

$$\begin{aligned} u^L(b) &= u^R(b) \\ u_x^L(b) &= u_x^R(b). \end{aligned} \tag{8}$$

We approximate the solution to (7) and (8) by a collocation method [1]. The equations on the subintervals $\Omega^L = [a, b]$ and $\Omega^R = [b, c]$ are each mapped onto the interval $[-1, 1]$ according to the transformations

$$\begin{aligned} X^L &= 2(x-a)/(b-a) - 1, \qquad x \in \Omega^L \\ X^R &= 2(x-b)/(c-b) - 1, \qquad x \in \Omega^R. \end{aligned} \tag{9}$$

On each subdomain, we define a grid, $\{X_j^L\}_{j=0}^{N^L}$, using $N^L + 1$ points on the left and, $\{X_j^R\}_{j=0}^{N^R}$, using $N^R + 1$ points on the right. The distribution of the grid points within each subdomain is given by the nodes of a Gauss–Lobatto quadrature rule. The solution unknowns are taken to be the vectors $\mathbf{U}^L$ and $\mathbf{U}^R$ whose components, $U_j^{L,R}$, are the approximate values of the solution at the grid points. Derivatives in the computational domains are computed by the matrix–vector product $\mathbf{DU}$, where $\mathbf{D}$ is the collocation derivative matrix. Explicit formulas for the Legendre and Chebyshev differentiation matrices can be found in [1]. To simplify the notation, we define the physical space derivative approximations by

$$\left(\frac{\partial^L \mathbf{U}^L}{\partial x}\right)_j \equiv X_x^L (\mathbf{D}^L \mathbf{U}^L)_j, \tag{10}$$

where X_x is the Jacobian of the transformation within the subdomain.

The semi-discrete collocation approximation in the two subdomains for all but the interface points is written as

$$\begin{aligned} U_0^L &= 0 \\ (U_t^L)_j &= \left(\frac{\partial^{2^L} U^L}{\partial x^2}\right)_j, \qquad j = 1, 2, \ldots, N^L - 1 \end{aligned} \tag{11a}$$

$$\begin{aligned} (U_t^R)_j &= \left(\frac{\partial^{2^R} U^R}{\partial x^2}\right)_j, \qquad j = 1, 2, \ldots, N^R - 1 \\ U_{N^R}^R &= 0. \end{aligned} \tag{11b}$$

We impose the interface continuity conditions, (8), weakly by integrating at the interface the equations

$$\begin{aligned} (U_t^L)_{N^L} = (U_t^R)_0 = \alpha \left(\frac{\partial^{2^L} \mathbf{U}^L}{\partial x^2}\right)_{N^L} + \beta \left(\frac{\partial^{2^R} \mathbf{U}^R}{\partial x^2}\right)_0 \\ + \delta \left(\left(\frac{\partial^R \mathbf{U}^R}{\partial x}\right)_0 - \left(\frac{\partial^L \mathbf{U}^L}{\partial x}\right)_{N^L}\right). \end{aligned} \tag{12}$$

The weights α, β, δ are given by

$$\begin{aligned} \alpha &= \frac{x_X^L w_{N^L}^L}{x_X^L w_{N^L}^L + x_X^R w_0^R}, \qquad \beta = \frac{x_X^R w_0^R}{x_X^L w_{N^L}^L + x_X^R w_0^R}, \\ \delta &= \frac{1}{x_X^L w_{N^L}^L + x_X^R w_0^R}. \end{aligned} \tag{13}$$

For the Legendre approximation, $w_0 = w_N = (N(N-1))^{-1}$ are the values of the Gauss–Lobatto quadrature weights at the endpoints of the interval.

The Legendre approximation given by (11), (12), and (13) is stable. To prove this, we multiply Eqs. (11a) by $U_j^L x_X^L w_j^L$ and (11b) by $U_j^R x_X^R w_j^R$. Equation (12) is multiplied by U_N^L/δ. The sum of these equations is

$$\begin{aligned} (U, U_t)_A &\equiv \sum_{j=0}^{N^L} U_j^L (U_t^L)_j x_X^L w_j^L + \sum_{j=0}^{N^R} U_j^R (U_t^R)_j x_X^R w_j^R \\ &= \sum_{j=0}^{N^L} U_j^L \left(\frac{\partial^{2^L} \mathbf{U}^L}{\partial x^2}\right)_j x_X^L w_j^L \\ &\quad + \sum_{j=0}^{N^R} U_j^R \left(\frac{\partial^{2^R} \mathbf{U}^R}{\partial x^2}\right)_j x_X^R w_j^R \\ &\quad + U_{N^L}^L \left(\left(\frac{\partial^R \mathbf{U}^R}{\partial x}\right)_0 - \left(\frac{\partial^L \mathbf{U}^L}{\partial x}\right)_{N^L}\right). \end{aligned} \tag{14}$$

The first sum on the right-hand side of (14) represents the Gauss quadrature of a polynomial of degree $2N - 1$. The second represents the quadrature of a polynomial of degree $2M - 1$. By the exactness of the Gauss–Lobatto quadrature

rule for such polynomials and by the definition of the collocation derivative, we can write (14) as

$$(U, U_t)_{\Delta} = \int_a^b U^{\mathrm{L}} U^{\mathrm{L}}_{xx}\, dx + \int_b^c U^{\mathrm{R}} U^{\mathrm{R}}_{xx}\, dx + U(b, t)(U^{\mathrm{R}}_x - U^{\mathrm{L}}_x)|_{x=b}, \tag{15}$$

where $U(x)$ is the polynomial interpolant through the solution values (cf. [1, p. 318]). The integrals in (15) can be integrated by parts and the boundary terms cancel. The result is

$$(U, U_t)_{\Delta} = -\|U_x\|^2_{\mathrm{L}^2}, \tag{16}$$

where we have used the L^2 norm

$$\|u\|^2_{\mathrm{L}^2(a,c)} = \int_a^b u^2\, dx + \int_b^c u^2\, dx.$$

The left-hand side of (16) bounds the L^2 norm of the energy [1]; that is,

$$(U, U_t)_{\Delta} \geqslant (U, U_t) = \frac{1}{2}\frac{d}{dt}\|U\|^2_{\mathrm{L}^2}.$$

Thus, the approximation is stable, i.e.,

$$\frac{1}{2}\frac{d}{dt}\|U\|^2_{\mathrm{L}^2} \leqslant -\|U_x\|^2_{\mathrm{L}^2} \leqslant 0 \tag{17}$$

Chebyshev approximations in the form (11) and (12) can also be used. For these approximations, the relevant quadrature is the Clenshaw–Curtis rule [1] and the number of points per subdomain must be odd. Funaro [15] indicates what modifications must be made for scalar equations to satisfy the technical details of the lower precision of the Clenshaw–Curtis rule. From a practical point of view, we have found little difference on a variety of one- and two-dimensional test problems between the stability of the Legendre approximation using the Gauss weights and the Chebyshev approximation using the Clenshaw–Curtis weights.

We consider two interface conditions for the approximation of the advection–diffusion equation

$$\begin{aligned} &u_t + u_x = \nu u_{xx}, \quad x \in [a, c], \quad \nu, t > 0 \\ &u(x, 0) = u_0(x) \\ &u(a, t) = u(c, t) = 0. \end{aligned} \tag{18}$$

The first condition uses the same weighted average of the advection terms as is used by the diffusion terms in Eq. (12),

$$\begin{aligned} (U^{\mathrm{L}}_t)_{N^{\mathrm{L}}} = (U^{\mathrm{R}}_t)_0 = \alpha &\left(\nu\left(\frac{\partial^2 \mathbf{U}^{\mathrm{L}}}{\partial x^2}\right)_{N^{\mathrm{L}}} - \left(\frac{\partial^{\mathrm{L}} \mathbf{U}^{\mathrm{L}}}{\partial x}\right)_{N^{\mathrm{L}}}\right) \\ &+ \beta\left(\nu\left(\frac{\partial^2 \mathbf{U}^{\mathrm{R}}}{\partial x^2}\right)_0 - \left(\frac{\partial^{\mathrm{R}} \mathbf{U}^{\mathrm{R}}}{\partial x}\right)_0\right) \\ &+ \delta\nu\left(\left(\frac{\partial^{\mathrm{R}} \mathbf{U}^{\mathrm{R}}}{\partial x}\right)_0 - \left(\frac{\partial^{\mathrm{L}} \mathbf{U}^{\mathrm{L}}}{\partial x}\right)_{N^{\mathrm{L}}}\right). \end{aligned} \tag{19}$$

For the linear, constant coefficient problem, (18), the same stability condition (17) holds for this interface algorithm.

The interface method (19) is conservative. Like the method in [4] this interface condition conserves the global flux when applied to an equation, possibly nonlinear, of the form

$$u_t + G_x = 0, \tag{20a}$$

where

$$G(u) = f(u) - \nu u_x. \tag{20b}$$

For Eq. (20), the interface approximation becomes

$$\begin{aligned} (U^{\mathrm{L}}_t)_{N^{\mathrm{L}}} = (U^{\mathrm{R}}_t)_0 = &-\alpha\left(\frac{\partial^{\mathrm{L}} \mathbf{G}}{\partial x}\right)_{N^{\mathrm{L}}} - \beta\left(\frac{\partial^{\mathrm{R}} \mathbf{G}}{\partial x}\right)_0 \\ &+ \delta\nu\left(\left(\frac{\partial^{\mathrm{R}} \mathbf{U}^{\mathrm{R}}}{\partial x}\right)_0 - \left(\frac{\partial^{\mathrm{L}} \mathbf{U}^{\mathrm{L}}}{\partial x}\right)_{N^{\mathrm{L}}}\right). \end{aligned} \tag{21}$$

To show conservation, the interior point equations are multiplied by the appropriate Gauss–Lobatto weights for the Legendre approximation and by the Clenshaw–Curtis weights for the Chebyshev approximation. The interface condition (21) is multiplied by $1/\delta$. The sum of the results is

$$\begin{aligned} &\sum_{j=0}^{N^{\mathrm{L}}} (U^{\mathrm{L}}_t)_j x^{\mathrm{L}}_X w^{\mathrm{L}}_j + \sum_{j=0}^{N^{\mathrm{R}}} (U^{\mathrm{R}}_t)_j x^{\mathrm{R}}_X w^{\mathrm{R}}_j \\ &\quad + \sum_{j=0}^{N^{\mathrm{L}}} \left(\frac{\partial^{\mathrm{L}} G^{\mathrm{L}}}{\partial x}\right)_j x^{\mathrm{L}}_X w^{\mathrm{L}}_j + \sum_{j=0}^{N^{\mathrm{R}}} \left(\frac{\partial^{\mathrm{L}} G^{\mathrm{R}}}{\partial x}\right)_j x^{\mathrm{R}}_X w^{\mathrm{R}}_j \\ &\quad - \nu\left(\left(\frac{\partial^{\mathrm{R}} \mathbf{U}^{\mathrm{R}}}{\partial x}\right)_0 - \left(\frac{\partial^{\mathrm{L}} \mathbf{U}^{\mathrm{L}}}{\partial x}\right)_{N^{\mathrm{L}}}\right) = 0. \end{aligned} \tag{22}$$

All the quadratures in (22) are exact, so we can write

$$\int_a^b U^{\mathrm{L}}_t\, dx + \int_b^c U^{\mathrm{R}}_t\, dx + \int_a^b G_x\, dx + \int_b^c G_x\, dx - \nu(U^{\mathrm{R}}_x - U^{\mathrm{L}}_x)|_{x=b} = 0 \tag{23}$$

or

$$\frac{d}{dt}\left[\int_a^b U^L\,dx+\int_b^c U^R\,dx\right]+[f(U^L)-\nu U_x^L]_a^b + [f(U^R)-\nu U_x^R]_b^c-\nu(U_x^R-U_x^L)|_{x=b}=0 \quad (24)$$

from which it follows that

$$\frac{d}{dt}\left[\int_a^b U^L\,dx+\int_b^c U^R\,dx\right]-G(a)+G(c)=0. \quad (25)$$

The difference between this interface condition and that of [4] is that (21) is computed only at the interface without needing to calculate global integrals.

The second interface condition to the advection–diffusion equation uses an *upwind* approximation to the advection terms at the interface,

$$(U_t^L)_{N^L}=(U_t^R)_0=-\left(\frac{\partial^L \mathbf{U}^L}{\partial x}\right)_{N^L}+\alpha\nu\left(\frac{\partial^{2^L}\mathbf{U}^L}{\partial x^2}\right)_{N^L} + \beta\nu\left(\frac{\partial^{2^R}\mathbf{U}^R}{\partial x^2}\right)_0+\delta\nu\left(\left(\frac{\partial^R \mathbf{U}^R}{\partial x}\right)_0-\left(\frac{\partial^L \mathbf{U}^L}{\partial x}\right)_{N^L}\right). \quad (26)$$

The upwind approximation has been shown to be stable and exponentially convergent for purely hyperbolic problems [5, 8, 9]. Unlike the approximation (19), it is not conservative, although the treatment of the viscous flux is conservative. Also, stability is not confirmed by the energy method. If (26) is used, the right-hand side of (16) is perturbed by a term that depends on the jump in the first derivative at the interface

$$\frac{1}{2}\frac{d}{dt}\|U\|_{L^2}^2=-\|U_x\|_{L^2}^2-U(b,t)\,w_0^R(U_x^L(b,t)-U_x^R(b,t)). \quad (27)$$

Nevertheless, one expects that the use of the upwind approximation of the advection terms is stable, as in the purely hyperbolic case.

As an example of the use of the interface conditions (19) and (26) we consider the advection dominated problem

$$\begin{aligned} &u_t+u_x=0.001u_{xx}+F, \qquad x\in[a,c], \quad \nu, t>0\\ &u(x,0)=0\\ &u(a,t)=1\\ &F(x)=\pi e^{\sin(\pi x)}(\cos(\pi x)-0.001\pi(\cos^2(\pi x)-\sin(\pi x)) \end{aligned} \quad (28)$$

which has the exact steady solution $u(x)=e^{\sin(\pi x)}$. Solutions were calculated on the interval $[0, 3]$ with four equally sized subdomains, $\Omega^k=[x_{\min}^k, x_{\max}^k]$, $k=1, 2, 3, 4$, with the same number of points in each. Figure 2 shows the error of the steady solution for the weighted average (19) and upwind (26) interface approximations measured in the $H^1(a, c)$ norm using the usual definition

$$\|U^k\|_{H^1(x_{\min}^k,x_{\max}^k)}^2=\int_{x_{\min}^k}^{x_{\max}^k}(U^k)^2\,dx+\int_{x_{\min}^k}^{x_{\max}^k}\frac{\partial(U^k)^2}{\partial x}\,dx$$

$$\|U\|_{H^1(a,c)}^2=\sum_k\|U^k\|_{H^1(x_{\min}^k,x_{\max}^k)}^2.$$

Both interface approximations show exponential convergence of the error in the H^1 norm. The upwind approximation is marginally more accurate than the other.

For system of equations,

$$\mathbf{Q}_t+\mathbf{A}\mathbf{Q}_x=\mathbf{B}\mathbf{Q}_{xx}, \qquad \mathbf{Q}\in\mathbb{R}^m, \quad \mathbf{A}, \mathbf{B}\colon \mathbb{R}^m\to\mathbb{R}^m, \quad (29)$$

the upwind interface can be implemented by a correction procedure as described by Kopriva [17, 5]. The correction for the advection terms can be written so that it does not affect the treatment of the viscous terms. It is applicable to both parabolic and incompletely parabolic equations.

To derive the correction method, we assume that the system (29) is constant coefficient and hyperbolic if $\mathbf{B}=\mathbf{0}$. In the case that the problem is not constant coefficient, a linearization such as that found in [5] can be done. Under these assumptions the matrix $\mathbf{A}$ is similar to a real diagonal

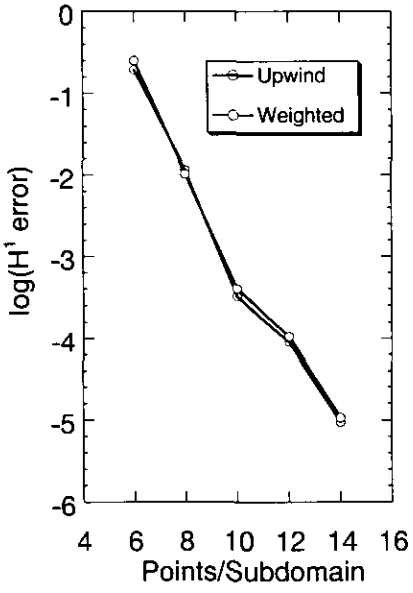

FIG. 2. Convergence of four-subdomain Legendre approximation to Eq. (28).

matrix, i.e., $\mathbf{A}=\mathbf{Z}\Lambda\mathbf{Z}^{-1}$. Then writing the system of equations as

$$\begin{aligned}\mathbf{Z}^{-1}[\mathbf{Q}_t+\mathbf{A}\mathbf{Q}_x-\mathbf{B}\mathbf{Q}_{xx}]\\ =\mathbf{Z}^{-1}\mathbf{Q}_t+\Lambda\mathbf{Z}^{-1}\mathbf{Q}_x-\mathbf{Z}^{-1}\mathbf{B}\mathbf{Q}_{xx}=0\end{aligned}\tag{30}$$

indicates that at an interface, the discrete solution, $\mathbf{Z}^{-1}\mathbf{Q}$, should be computed so that the first derivatives are evaluated according to the sign of the entries of Λ.

The procedure begins by computing two preliminary solutions, $\mathbf{Q}_L^*$ and $\mathbf{Q}_R^*$, one for each side of the interface. These solutions are computed by integrating

$$(\mathbf{Q}_t^L)_{N^L}=-\mathbf{A}\left(\frac{\partial^L\mathbf{Q}^L}{\partial x}\right)_{N^L}+\mathbf{V}\tag{31a}$$

and

$$(\mathbf{Q}_t^R)_0=-\mathbf{A}\left(\frac{\partial^R\mathbf{Q}^R}{\partial x}\right)_0+\mathbf{V},\tag{31b}$$

where

$$\begin{aligned}\mathbf{V}=\mathbf{B}\Bigg[\alpha\left(\frac{\partial^{2^L}\mathbf{Q}^L}{\partial x^2}\right)_{N^L}+\beta\left(\frac{\partial^{2^R}\mathbf{Q}^R}{\partial x^2}\right)_0\\ +\delta\left(\left(\frac{\partial^R\mathbf{Q}^R}{\partial x}\right)_0-\left(\frac{\partial^L\mathbf{Q}^L}{\partial x}\right)_{N^L}\right)\Bigg].\end{aligned}\tag{31c}$$

The preliminary solutions are then corrected to account for the propagation of waves moving through the interface. From (30), the entries of $\mathbf{Z}^{-1}\mathbf{Q}$ correspond to characteristic variables associated with the positive and negative eigenvalues of $\mathbf{A}$. Suppose we decompose the preliminary solution vectors by

$$\begin{bmatrix}W_L^+\\ W_L^-\end{bmatrix}=\mathbf{Z}^{-1}\mathbf{Q}_L^*,\qquad \begin{bmatrix}W_R^+\\ W_R^-\end{bmatrix}=\mathbf{Z}^{-1}\mathbf{Q}_R^*,\tag{32}$$

where W^+ represents right-going waves and W^- represents left-going waves. Then the corrected solution, $\mathbf{Q}^c$, is reconstructed from W_L^+ and W_R^- by

$$\mathbf{Q}_L^c=\mathbf{Q}_R^c=\mathbf{Z}\begin{bmatrix}W_L^+\\ W_R^-\end{bmatrix}.\tag{33}$$

As an example of the solution of a parabolic system, we consider the steady solution to

$$\begin{bmatrix}u\\ v\end{bmatrix}_t+\begin{bmatrix}1 & 2\\ 2 & 1\end{bmatrix}\begin{bmatrix}u\\ v\end{bmatrix}_x=0.001\begin{bmatrix}1 & 1\\ 1 & 1\end{bmatrix}\begin{bmatrix}u\\ v\end{bmatrix}_{xx}+\mathbf{F},$$

$$x\in[-1,1],\quad t>0$$

$$\begin{bmatrix}u(x,0)\\ v(x,0)\end{bmatrix}=\mathbf{0}\tag{34}$$

$$\begin{aligned}u(-1,t)+v(-1,t)&=1+e\\ u(1,t)-v(1,t)&=1-e^{-1}\\ u_x(-1,t)+v_x(-1,t)&=-\pi-e\\ u_x(1,t)+v_x(1,t)&=-\pi-e^{-1}.\end{aligned}\tag{35}$$

The forcing term, $\mathbf{F}$, is chosen so that the exact steady solution is

$$\begin{aligned}u(x)&=e^{\sin(\pi x)}\\ v(x)&=e^{-x}.\end{aligned}$$

The hyperbolic part of this system has two waves $W^{\pm}=u\pm v$ that travel at speeds $+3$ and -1, respectively. This leads to the first two boundary conditions (35) which are also implemented by the correction procedure. The second two equations represent conditions required by the viscous terms. They are imposed weakly, i.e., when calculating the diffusion terms [1, p. 88]. A three-stage Runge–Kutta was used to integrate the semi-discrete equations in time.

The steady solution to (34) and (35) is shown in Fig. 3 for a Legendre calculation with four subdomains of equal size and 10 points per subdomain. The computed results shown are those of the weighted scheme for the advection terms. The solutions for the upwind interface condition look identical on the graph.

The error decays exponentially fast for both the weighted and the characteristic interface schemes. Figure 4 shows the error of u and v in the H^1 norm as a function of the number of points per subdomain. Again, four equal size subdomains were used for these calculations.

It might appear that there is little advantage to be gained from the extra work required by the characteristic interface condition, but this is not the case for the advection dominated steady solutions that often occur in practice. Figure 5 shows the maximum residual as a function of time step (iteration) for eight points per subdomain. The time step was chosen individually to give the highest convergence

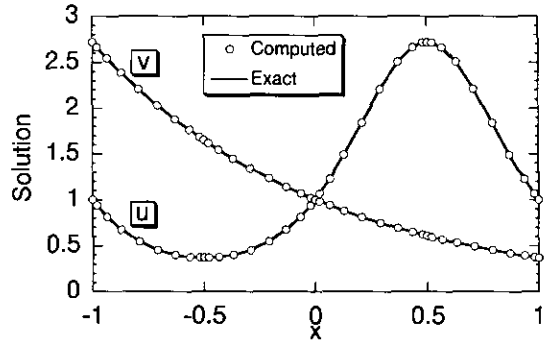

FIG. 3. Solution of the linear parabolic system (34) using four subdomains.

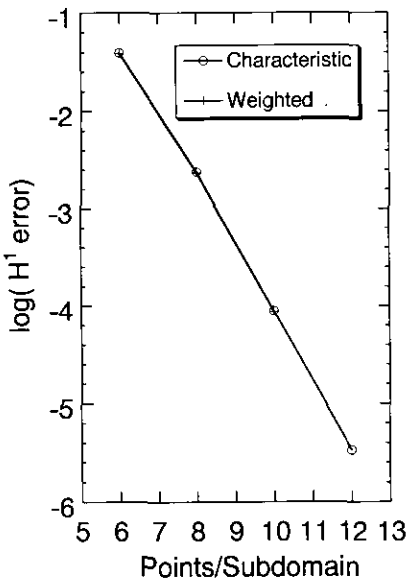

FIG. 4. Convergence of the error for the linear parabolic system (34).

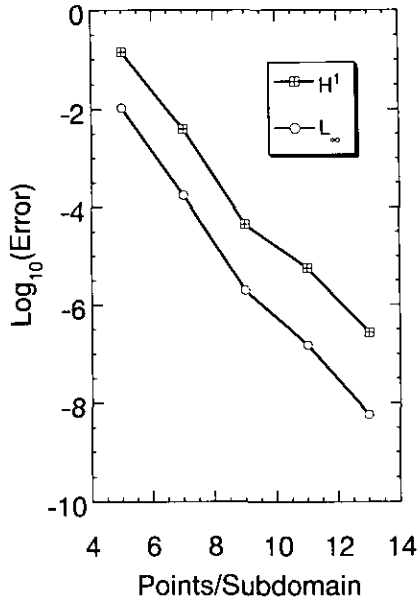

FIG. 6 Convergence of the Chebyshev approximation to Eq. (34).

rate for each interface method. In this example, the solution using the weighted scheme would take approximately an order of magnitude more work to converge to steady state. For this reason, we prefer the characteristic treatment of the advection terms at the interfaces for the computation of steady flows.

The Chebyshev approximation with the characteristic interface condition is also convergent and spectrally accurate. Figure 6 shows the H^1 and maximum errors for the same case as in Fig. 4. The decay of the error is exponential and tracks the decay of the coefficients of the Chebyshev interpolant of u. The Chebyshev approximation is more accurate than the Legendre approximation by a factor of 3.3 at 12 points per subdomain.

The method is also exponentially convergent when applied to an incompletely parabolic system. As an example, we consider the problem (34) with the matrix

$$\mathbf{B}=\begin{bmatrix}1 & 0\\ 0 & 0\end{bmatrix}. \tag{36}$$

This case is closer to the Navier–Stokes situation, where the density equation does not have a dissipation term. Exponential convergence of the error is demonstrated in Fig. 7.

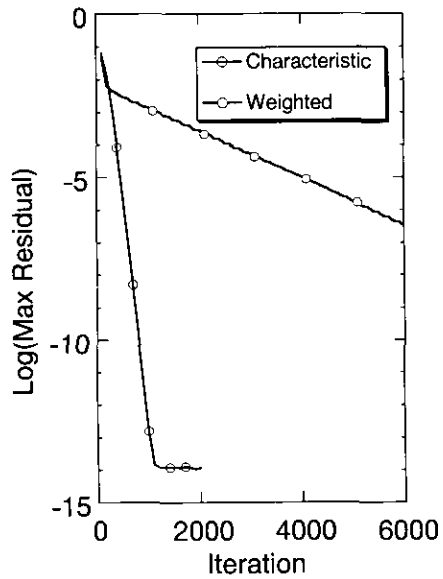

FIG. 5. Convergence to steady state of the system (34) for the two interface conditions.

3.2. Burgers' Equation with a Viscous Shock

The next test case is an application of the method to a nonlinear problem in which a near viscous shock appears. The problem is to solve the equation

$$\begin{aligned}&\frac{\partial u}{\partial t}+u\frac{\partial u}{\partial x}=\nu\frac{\partial^2 u}{\partial x^2}, \qquad |x|\leqslant 1, \quad t>0\\ &u(\pm 1, t)=0\\ &u(x,0)=-\sin(\pi x)\end{aligned} \tag{37}$$

with $\nu=10^{-2}/\pi$. For this problem, the solution steepens to a sawtooth wave with a very steep, yet continuous, profile at $x=0$. The maximum slope at the origin is reached near $t=0.5$, after which time that slope decreases. This problem

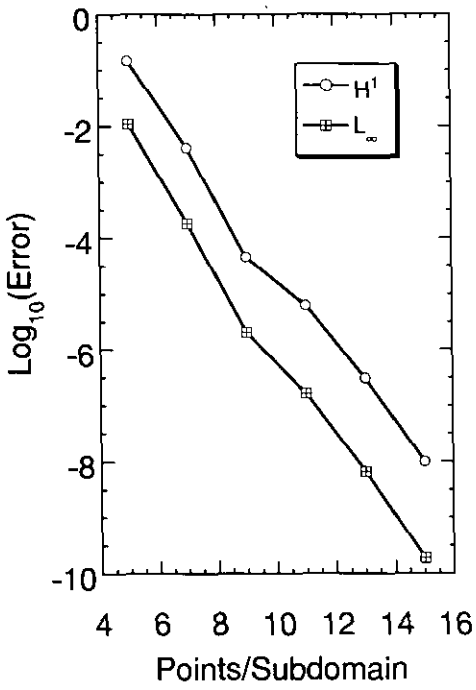

FIG. 7. Convergence of the Chebyshev approximation to a linear, incompletely parabolic system with diffusion matrix (36).

was used by Basdevant *et al.* [18] to compare several discretization techniques, including Fourier and Chebyshev spectral methods, a finite difference method, and the spectral element method.

We solved (37) on four subdomains with interfaces located at $x=-0.05$, $x=0.0$, and $x=+0.05$ and 17 grid points per subdomain. These are the same parameters used in the spectral element solution to the problem. Figure 8 shows the solution at the three times, $t=0$, $t=1/\pi$, and $t=2/\pi$. Unlike the single domain Chebyshev spectral method with double the number of grid points ($N=128$, see [18]), the multidomain solution is oscillation-free due to the fine resolution of the solution near the viscous shock.

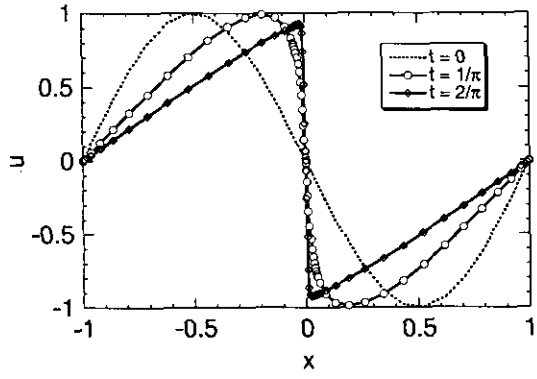

FIG. 8. Solution to Burgers' equation at three different times, using four subdomains.

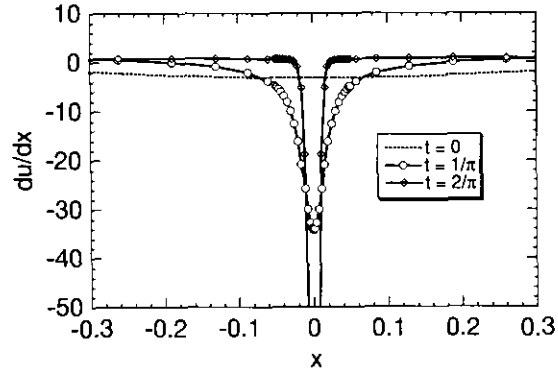

FIG. 9. First derivative of the solution to Burgers' equation using four subdomains.

The solution remains continuous and smooth through the interfaces as the solution develops over this time interval.

The first derivative of the solution is also continuous and smooth through the viscous shock. Figure 9 shows the first derivative of the solution near $x=0$ at the same times as in Fig. 8. Note also that the derivative is smooth through the interfaces. In [18] the exact value of the maximum slope was computed to be 152.00516 at $t=1.6/\pi=0.509$. We found $|\partial u/\partial x|_{\max}=152.04$ to five significant digits. This result is identical to the spectral element result and is significantly better than the value of 145.877 obtained by single domain Chebyshev collocation with 512 points. One difference between the new method and the spectral element method is that the new method does not need to invert a mass matrix to update the solution. If we increase the number of points from 17 to 19 per subdomain, the absolute error decreases by almost two orders of magnitude from 3.8×10^{-2} to 5×10^{-4}.

3.3. Viscous flow in a Quasi-One-Dimensional Nozzle

As an example of the application of the ideas presented above to the Navier–Stokes equations, we consider the flow in a quasi-one-dimensional converging-diverging nozzle. The density, velocity, and pressure satisfy the equations

$$\begin{aligned}
&\rho_t+\rho u_x+u\rho_x+\rho u\frac{A_x}{A}=0\\
&u_t+uu_x+\frac{1}{\rho}p_x=\frac{\sqrt{\gamma}}{\rho\,\mathrm{Re}}\left(\frac{4}{3}\frac{\partial}{\partial x}(\mu u_x)+\frac{4}{3}\mu u_x\frac{A_x}{A}\right)\\
&p_t+up_x+\gamma p\left(u_x+\frac{uA_x}{A}\right)\\
&\quad=\frac{\gamma\sqrt{\gamma}}{\mathrm{Pr}\,\mathrm{Re}}\left((\kappa T_x)_x+\frac{\kappa T_x A_x}{A}\right)+\frac{(\gamma-1)\sqrt{\gamma}}{\mathrm{Re}}\left(\frac{4}{3}\mu u_x^2\right).
\end{aligned}\tag{38}$$

These equations can be derived from (1) and (2) by setting v and all y derivatives equal to zero and by using the fact

that for an area variation $A(x)$, the quasi-one-dimensional divergence of some flux, $\mathbf{f}=(f, 0)$, is

$$\nabla \cdot \mathbf{f}=\frac{\partial(fA)}{\partial x}.$$

The reference quantities are chosen to be the values at the throat. We use the area variation $A(x)=x/2+1/x$, which has its throat at $x=\sqrt{2}$.

At the inflow, we specify the density and the incoming Riemann invariant from the inviscid solution,

$$\begin{aligned} \rho &= \rho_{\text{in}} \\ R^+ &= p_{\text{in}}+\rho_{\text{in}} a_{\text{in}} u_{\text{in}}. \end{aligned} \tag{39}$$

The extra boundary conditions required by the presence of the viscous terms can be applied indirectly by modifying the viscous fluxes as necessary (see, e.g., [19]). The inflow pressure and the velocity are computed using a correction procedure. At the outflow, no inviscid boundary condition is specified. For the initial condition, we use the exact solution to the inviscid problem with a perturbation in the pressure at one of the grid points in the subsonic portion of the nozzle.

The nozzle is divided into multiple subdomains, $\Omega_k=[x_{\min}(k),\ x_{\max}(k)]$. On each subdomain, Eqs. (38) are mapped from the interval $[x_{\min}(k), x_{\max}(k)] \leftrightarrow [0, 1]$ by

$$X^k=\frac{x-x_{\min}(k)}{x_{\max}(k)-x_{\min}(k)}.$$

The interior point equations are then approximated in the usual way by either Chebyshev or Legendre collocation.

The interface conditions use a weighted average for the viscous terms computed from both sides, with a penalty added for the jump in the viscous fluxes described above. The solutions are updated using the midpoint rule and are corrected for the inviscid characteristics.

We detail the interface procedure below. For simplicity of exposition, we write Eqs. (38) in the vector form $\mathbf{Q}_t+\mathbf{A}=\mathbf{V}$, where $\mathbf{Q}=[\rho u p]^{\mathrm{T}}$, $\mathbf{A}$ represents the advective terms, and $\mathbf{V}$ represents the viscous terms. For this discussion, we will use the forward Euler scheme for the time integration. We will also assume that subdomains are ordered from left to right in increasing order.

The interior points of each subdomain are updated using

$$\mathbf{Q}_j^{k,n+1}=\mathbf{Q}_j^{k,n}+\Delta t[-\mathbf{A}_j^{k,n}+\mathbf{V}_j^{k,n}], \tag{40}$$

where $\mathbf{A}_j^{k,n}$ and $\mathbf{V}_j^{k,n}$ represent the collocation approximations of the advective and diffusion terms at the grid point j on subdomain k at time level n.

Preliminary values of the solution at the interface are obtained by solving the equations

$$\begin{aligned} \mathbf{Q}_{N^k}^{k,*} &= \mathbf{Q}_{N^k}^{k,n}+\Delta t[-\mathbf{A}_{N^k}^{k,n}+\alpha \mathbf{V}_{N^k}^{k,n}+\beta \mathbf{V}_0^{k+1,n} \\ &\quad +\delta(\mathbf{F}_0^{k+1,n}-\mathbf{F}_{N^k}^{k,n})] \\ \mathbf{Q}_0^{k+1,*} &= \mathbf{Q}_0^{k+1,n}+\Delta t[-\mathbf{A}_0^{k+1,n}+\alpha \mathbf{V}_{N^k}^{k,n}+\beta \mathbf{V}_0^{k+1,n} \\ &\quad +\delta(\mathbf{F}_0^{k+1,n}-\mathbf{F}_{N^k}^{k,n})], \end{aligned} \tag{41}$$

where the viscous flux vector is

$$\mathbf{F}=\left[0 \quad \frac{4\sqrt{\gamma}}{3\rho\,\mathrm{Re}}\mu\frac{\partial u}{\partial x} \quad \frac{\gamma\sqrt{\gamma}}{\mathrm{Pr}\,\mathrm{Re}}\kappa\frac{\partial T}{\partial x}\right]^{\mathrm{T}}.$$

The weights α, β, δ are defined in Eq. (13).

The preliminary values of p, ρ, and u are corrected according to the inviscid characteristics. For the flow moving left to right, we define the linearized Riemann variables

$$\begin{aligned} R^+ &= p_{N^k}^{k,*}+\rho^n a^n u_{N^k}^{k,*} \\ R^- &= p_0^{k+1,*}-\rho^n a^n u_0^{k+1,*} \\ S_0 &= p_{N^k}^{k,*}-\rho_{N^k}^{k,*}(a_{N^k}^n)^2 \end{aligned} \tag{42}$$

which assume that the basic flow is from left to right. The corrected values are then computed by

$$\begin{aligned} p_{N^k}^{k,n+1} &= p_0^{k+1,n+1}=\frac{1}{2}(R^++R^-) \\ u_{N^k}^{k,n+1} &= u_0^{k+1,n+1}=\frac{1}{2\rho^n a^n}(R^+-R^-) \\ \rho_{N^k}^{k,n+1} &= \rho_0^{k+1,n+1}=\frac{1}{(a^n)^2}(p_{N^k}^{k,n+1}-S_0). \end{aligned} \tag{43}$$

Note that this correction does not affect the treatment of the viscous terms, since they are computed identically on each side of the interface.

As an example of the performance of the approximation, we consider the Chebyshev solution for $\mathrm{Re}=750$ and $\mathrm{Pr}=0.72$. There is no exact solution, so we compare the solution to a single domain calculation. Figure 10 compares the steady pressure, temperature, and velocity of a four-domain decomposition with those of a single-domain solution computed with the same total number of grid points. The convergence to steady state in 64-bit precision is shown in Fig. 11. In that figure, we define a work unit to be the CPU time of one time step of the single domain calculation using the same total number of grid points as the multi-

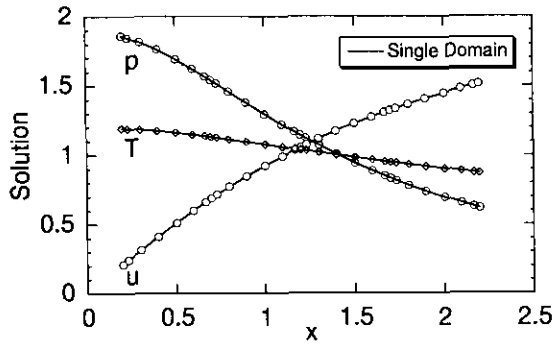

FIG. 10. Computed solution for transonic flow in a quasi-one-dimensional nozzle.

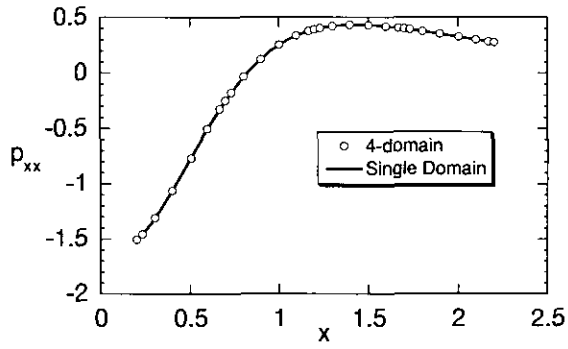

FIG. 12. Second derivative of the pressure in the converging–diverging nozzle.

domain calculation. The convergence of the single domain calculation is also included on Fig. 11 for comparison.

The interface condition ensures only that the solution be continuous at the interfaces. The continuity of the first derivative is enforced weakly. In general, there will be a jump discontinuity in the second derivative as well at an interface. However, that jump decays exponentially fast as the grid is refined when approximations of equal accuracy are used in each subdomain. Figure 12 shows a plot of the second derivative of the pressure for the four subdomain decomposition with eight points per subdomain compared to a single domain calculation with the same total number of points. Out of the three interfaces, the largest jump in this case is 5×10^{-4}, which is too small to see on the graph. The convergence of the largest jump with grid resolution is exponential as shown in Fig. 13.

3.4. Linear, Two-Dimensional Problems

The algorithm described in the previous section can be extended naturally to two space dimensions. The correction procedure for the advection terms in two dimensions can be found in [5] so we will describe only the treatment of the diffusion terms here. In this paper we consider nonoverlapping and "conforming" approximations only. By conforming we mean that grid lines must be aligned between subdomains. We will relax this requirement in a later paper.

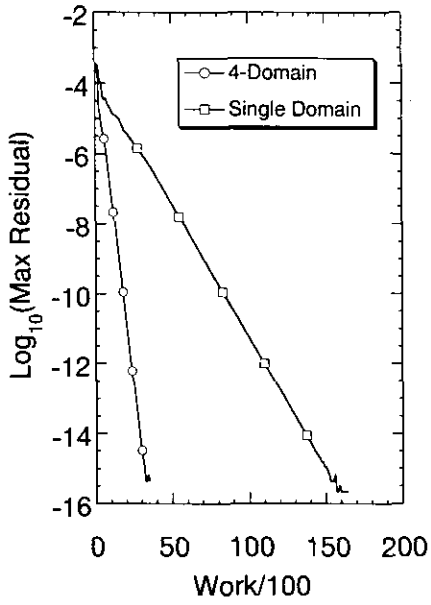

FIG. 11. Convergence to steady state of the four-doman and single-domain solutions.

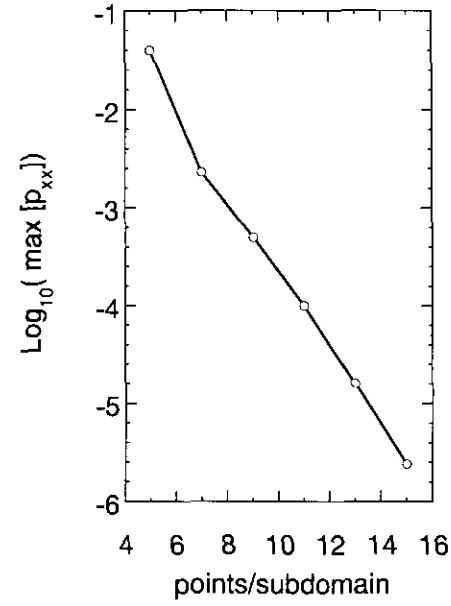

FIG. 13. Convergence of the interface value of the jump in the second derivative of the pressure with grid resolution.

We begin by considering the solution of the time dependent problem

$$\begin{aligned} u_t &= F_x + G_y, \qquad (x, y) \in \Omega \subset \mathbb{R}^2 \\ F &= u_x, \qquad G = u_y \\ u(x, y, 0) &= u_0 \\ u &= 0, \qquad (x, y) \in \partial\Omega \end{aligned} \tag{44}$$

on two domains as shown in Fig. 14. According to the *restriction on the grid lines, each subdomain contains* M grid points in the vertical direction. They can have different numbers of grid points in the horizontal direction as necessary.

Under the mapping $(x, y) \in \Omega \to (X, Y) \in \tilde{\Omega} = [-1, 1] \times [-1, 1]$, the differential equation in (44) becomes

$$u_t = (\tilde{F}_X + \tilde{G}_Y)/J, \tag{45a}$$

where

$$\begin{aligned} \tilde{F} &= y_Y F - x_Y G \\ \tilde{G} &= -y_X F + x_X G \\ J &= x_X y_Y - x_Y y_X. \end{aligned} \tag{45b}$$

The two-dimensional approximation is derived from the two-dimensional Gauss quadrature

$$\int_{-1}^{1}\int_{-1}^{1} U(X, Y)\, dX\, dY \approx \sum_{i=0}^{N}\sum_{j=0}^{M} U_{i,j} w_i \eta_j \tag{46}$$

which is exact for polynomials, $U(X, Y)$, that are of degree less than or equal to $2N-1$ in X and $2M-1$ in Y. At the interior points, we approximate the equations in the usual manner,

$$\frac{dU_{i,j}^{(\mathrm{L,R})}}{dt} = \frac{1}{J_{i,j}^{(\mathrm{L,R})}} (D_X^{\mathrm{L,R}}[\tilde{F}^{\mathrm{L,R}}] + D_Y^{\mathrm{L,R}}[\tilde{G}^{\mathrm{L,R}}])_{i,j}, \tag{47}$$

where $D_X^{\mathrm{L,R}}[\tilde{F}]_{i,j}$ is the two-dimensional spectral collocation derivative at (X_i, Y_j). At the points along the interface, we solve

$$\begin{aligned} \frac{dU_{N^{\mathrm{L}},j}^{\mathrm{L}}}{dt} = \frac{dU_{0,j}^{\mathrm{R}}}{dt} &= \alpha_j \left(\frac{1}{J^{\mathrm{L}}} (D_X^{\mathrm{L}}[\tilde{F}^{\mathrm{L}}] + D_Y^{\mathrm{L}}[\tilde{G}^{\mathrm{L}}]) \right)_{N^{\mathrm{L}},j} \\ &+ \beta_j \left(\frac{1}{J^{\mathrm{R}}} (D_X^{\mathrm{R}}[\tilde{F}^{\mathrm{R}}] + D_Y^{\mathrm{R}}[\tilde{G}^{\mathrm{R}}]) \right)_{0,j} \\ &+ \delta_j (\tilde{F}_{0,j}^{\mathrm{R}} - \tilde{F}_{N^{\mathrm{L}},j}^{\mathrm{L}}) \end{aligned} \tag{48}$$

for $j = 1, 2, \ldots, M-1$. The interface approximation is a weighted average of the diffusion terms plus a penalty proportional to the jump in the normal diffusive flux. In this case, the weights depend on the index j:

$$\begin{aligned} \alpha_j &= \frac{J_{N^{\mathrm{L}},j}^{\mathrm{L}} w_{N^{\mathrm{L}}}^{\mathrm{L}}}{J_{N^{\mathrm{L}},j}^{\mathrm{L}} w_{N^{\mathrm{L}}}^{\mathrm{L}} + J_{0,j}^{\mathrm{R}} w_0^{\mathrm{R}}}, \qquad \beta_j = \frac{J_{0,j}^{\mathrm{R}} w_0^{\mathrm{R}}}{J_{N^{\mathrm{L}},j}^{\mathrm{L}} w_{N^{\mathrm{L}}}^{\mathrm{L}} + J_{0,j}^{\mathrm{R}} w_0^{\mathrm{R}}}, \\ \alpha_j &= \frac{1}{J_{N^{\mathrm{L}},j}^{\mathrm{L}} w_{N^{\mathrm{L}}}^{\mathrm{L}} + J_{0,j}^{\mathrm{R}} w_0^{\mathrm{R}}}. \end{aligned} \tag{49}$$

Subdomain decompositions with corner points can be handled in a similar manner. Consider the four domain decomposition shown in Fig. 15. The interior points and vertical interface points are computed by (47) and (48). Horizontal interface points are computed by the formula analogous to (48). At the corner point, we integrate

$$\begin{aligned} \frac{dU}{dt} = \sum_{l=1}^{4} \alpha_l \frac{1}{J^l} (D_X^l[\tilde{F}] + D_Y^l[\tilde{G}]) \\ + \delta_{12}[\tilde{F}^2 - \tilde{F}^1] + \delta_{34}[\tilde{F}^4 - \tilde{F}^3] \\ + \delta_{13}[\tilde{G}^3 - \tilde{G}^1] + \delta_{24}[\tilde{G}^4 - \tilde{G}^2]. \end{aligned} \tag{50}$$

We have left off the subscripts that denote which grid point is used in the respective subdomains. This time, the interface point is computed as a weighted average of the diffusion terms in all four subdomains plus penalties proportional to

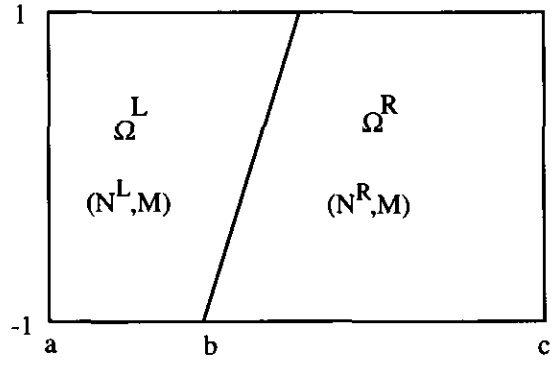

FIG. 14. A two-domain decomposition with M points in the vertical direction.

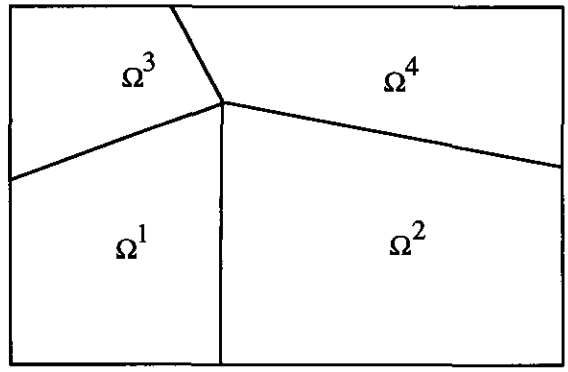

FIG. 15. A four-domain problem with a corner interface point.

the jumps in the four normal diffusive fluxes at the point. The weight functions are

$$\alpha_k = \frac{\omega^k \eta^k}{\sum_{j=1}^4 w^j \eta^j}, \quad \delta_{12} = \frac{\eta^1}{\sum_{j=1}^4 w^j \eta^j}, \quad \delta_{13} = \frac{\omega^1}{\sum_{j=1}^4 w^j \eta^j},$$
$$\delta_{24} = \frac{\omega^2}{\sum_{j=1}^4 w^j \eta^j}, \quad \delta_{34} = \frac{\eta^3}{\sum_{j=1}^4 w^j \eta^j}; \tag{51}$$

For the Legendre collocation method, w^k and η^k are the endpoint Gauss quadrature weights for the subdomain k. For Chebyshev collocation they are the Clenshaw–Curtis weights. The proof for stability of the Legendre approximation is similar to the one-dimensional case.

As an example of the use of the method, we solve the advection–diffusion equation

$$\begin{aligned} u_t + 0.3u_x + 0.6u_y &= 0.1(u_{xx} + u_{yy}) + f(x, y), \\ &(x, y) \in \Omega = [0, 1.2] \times [0, 1.2] \\ u(x, y, t) &= u_b(x, y), \qquad (x, y) \in \partial\Omega \\ u(x, y, 0) &= 0, \end{aligned} \tag{52}$$

where $f(x, y)$ and the boundary data were chosen so that the exact steady solution is

$$u(x, y) = \tfrac{1}{2}(e^{-10((x-0.8)^2 + (y-0.6)^2)} + e^{-10((x-0.3)^2 + (y-0.4)^2)}). \tag{53}$$

With these parameters, the relative importance of the advective and diffusion terms varies over the domain. The diffusion terms dominate near the peaks of the solution. Around the steepest gradients, advection dominates. Elsewhere are regions where the advection and diffusion terms have roughly the same magnitude.

To solve (52), we subdivide Ω into nine subdomains that are each mapped onto the unit square by bilinear transformations. The interface algorithms (48) and (50) were used for the viscous terms. The advection terms were computed with the upwind condition. Figure 16 shows the Chebyshev solution with 11 points per subdomain and the corresponding nine subdomain grid. Exponential convergence of the error as a function of the number of points per subdomain is shown in Fig. 17.

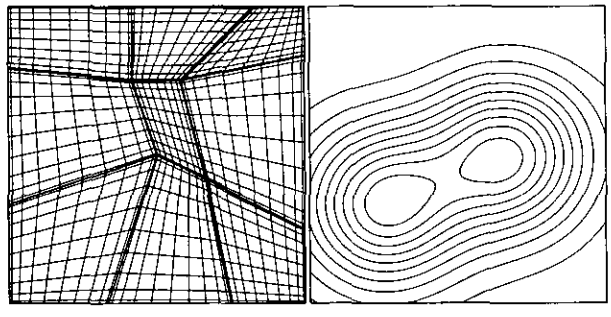

FIG. 16 Grid and solution for problem (52).

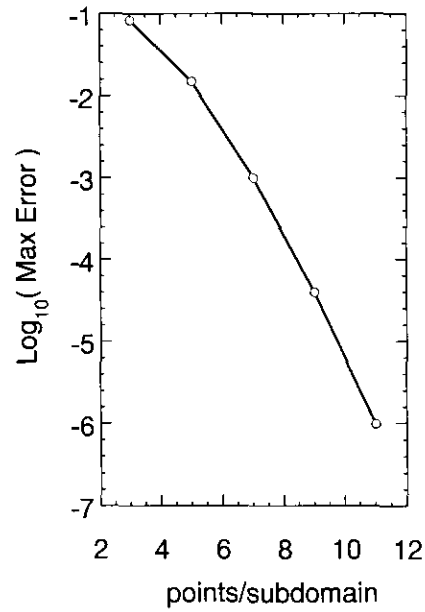

FIG. 17 Convergence of the maximum error of the nine subdoain Chebyshev solution to Eq. (52).

4. APPLICATIONS

To demonstrate the use of the method on two-dimensional flow problems, we consider two compressible flows over a flat plate, plus a transonic flow in a two-dimensional converging–diverging nozzle. For the flat plate problems, boundary layer solutions are computed for a subsonic flow over an isothermal plate and a supersonic flow over an adiabatic plate. The nozzle flow gives an example with a more complicated geometry where rapid changes in the flow direction near the throat require extra resolution, in addition to the necessity to resolve the boundary layer.

4.1. Compressible Flow over a Flat Plate

The first flat plate problem is the $M = 2$ supersonic flow over an adiabatic plate at $\mathrm{Re} = 10{,}000$. The second is the $M = 0.6$ subsonic flow over a $T = 2$ isothermal plate at $\mathrm{Re} = 2500$. In both problems, $\mathrm{Pr} = 0.72$ was used. The results are compared to the solutions of the spectral compressible boundary layer code of [20].

4.1.1. *Boundary Conditions*

The viscous boundary conditions were treated as described in [19]. To solve the flat plate problems, we must treat subsonic and supersonic inflow and outflow, a free-

stream condition at the top boundary, and adiabatic or isothermal wall conditions at the plate.

At subsonic inflow points along the left boundary, we specify the incoming normal Riemann invariant, the density, and the vertical velocity component using the compressible boundary layer result as the input profile. The pressure and streamwise velocity component are computed by a compatibility equation. Since the flow is not strongly varying in the streamwise direction, we set the viscous terms to zero at the inflow. At supersonic inflow points, all flow quantities are specified. The upper boundary is treated as subsonic outflow in the direction normal to the boundary since the vertical velocity in the boundary layer flow is positive.

At the supersonic outflow points, no inviscid condition is required. We can treat the viscous condition by setting the normal derivatives of the velocity and the temperature to zero before computing the viscous terms. At subsonic outflow points, one more boundary condition must be specified. For the calculations presented here, we specify the pressure to be the boundary layer value, $p = 1$. We use a streamwise compatibility condition (cf. Eq. (30)) to determine the streamwise velocity. The compatibility condition between the pressure and the velocity for the normal direction is

$$p_t + R_p + \rho a\{u_t + R_u\} = 0, \tag{54}$$

where R_p and R_u are the spatial derivative terms for the pressure and u-velocity equations in (1). The velocity in the direction tangential to the boundary is computed from the interior. With p specified and constant in time, $p_t = 0$, Eq. (54) leads to the outflow equation

$$u_t = -(R_u + R_p/\rho a) \tag{55}$$

that is discretized and integrated in the same manner as are the interior points. For the density, we discretize and integrate the locally one-dimensional compatibility equation

$$\rho_t = -\left\{\frac{1}{a^2} V_p + u\left(\rho_x - \frac{1}{a^2} p_x\right)\right\}, \tag{56}$$

where V_p represents the viscous terms of the pressure equation.

To compute the wall pressure, we solve a compatibility equation that relates the pressure and the normal velocity along the inviscid characteristic direction. For the adiabatic case, we impose the temperature boundary condition indirectly (see [1, 19]) through the thermal diffusion terms in the pressure equation. Then the compatibility equation between the pressure and the normal momentum at the plate is

$$p_t + R_p - \rho a\{v_t + R_v\} = 0. \tag{57}$$

Application of the no-slip boundary condition yields an equation for the pressure

$$p_t + R_p - \rho a R_v = 0 \tag{58}$$

that is discretized and integrated in the same manner as are the interior point equations.

The method used to compute the density at the plate surface from the pressure depends on whether the surface is isothermal or adiabatic. For an isothermal wall, the density is calculated directly from the pressure by the equation of state, Eq. (4). For the adiabatic case we use the first of the two methods studied in [19].

The method we use for the adiabatic surface condition computes the density so that at the plate it explicitly satisfies the thermal boundary condition. The adiabatic condition gives a relationship between the normal derivatives of the pressure and the density,

$$\frac{\partial \rho}{\partial N} = \frac{\rho}{p}\frac{\partial p}{\partial N}. \tag{59}$$

Once the pressure is computed by the compatibility condition, (58), its normal derivative can be computed. The wall density is then computed so that the (59) is satisfied. To be specific, consider a one-dimensional problem with M collocation points and no mappings. The density derivative is set to

$$\sum_{m=0}^{M} d_{0,m}\rho_m = \rho_0\left(\frac{1}{p}\frac{\partial p}{\partial y}\right)_{\text{plate}}, \tag{60}$$

where ρ_0 is the value at the plate and (d_{ij}) are the elements of the collocation derivative matrix. Equation (60) is a linear equation in ρ_m from which ρ_0 can be found,

$$\rho_0 = \frac{\sum_{m=1}^{M} d_{0,m}\rho_m}{((1/p)(\partial p/\partial y))_{\text{plate}} - d_{0,0}}. \tag{61}$$

4.1.2. *Results*

The flows were computed in a rectangular region $\Omega = [0.4, 2.8] \times [0.0, 0.4]$. For the examples presented here, we subdivided the region into nine subdomains, each mapped onto a unit square by a bilinear transformation. Vertical interfaces were placed at $x = 1.0$ and $x = 1.8$. The locations of the interfaces in the streamwise direction were chosen to

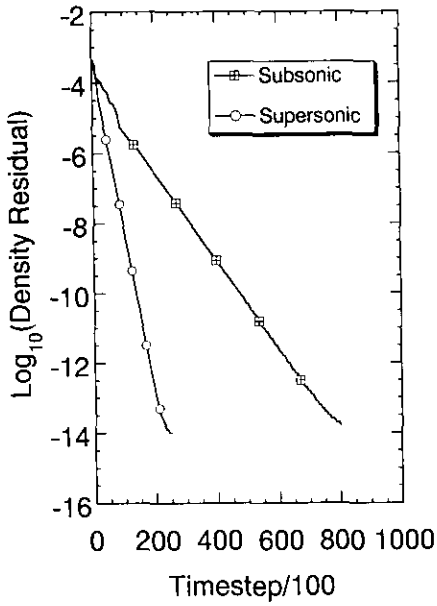

FIG. 18. Convergence to steady state of the subsonic and supersonic flow solutions.

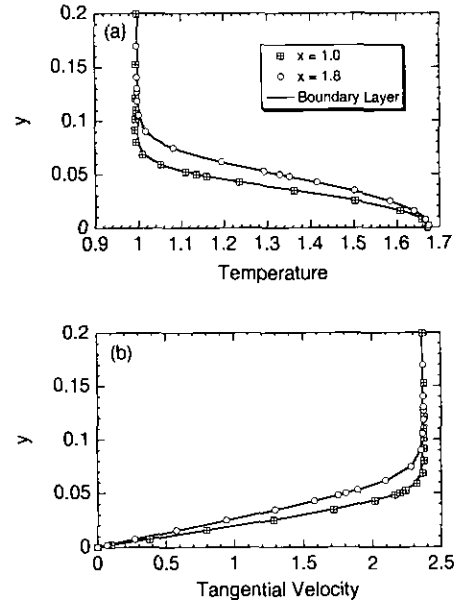

FIG. 20. Temperature (a) and tangential velocity (b) profiles along the vertical interfaces for the $M = 2$ boundary layer flow.

fall in a variety of flow regimes and to roughly follow the growth of the boundary layer down the length of the plate. Nine points were used in each direction in each subdomain.

Convergence behavior to steady state for both the supersonic and subsonic flow examples is shown in Fig. 18. In both cases it was possible to converge the density residual to *double precision machine zero.*

The velocity vectors, temperature contours, and grid for the $M = 2$ supersonic flow over the adiabatic flat plate at $\mathrm{Re} = 10{,}000$ are shown in Fig. 19. Superimposed on the velocity vector plot are contours representing the sonic line and the edge of the boundary layer. With this choice of subdomains, the streamwise interfaces fall in supersonic parts of the boundary layer. Profiles of the temperature and tangential velocity along the two vertical interfaces are shown in Fig. 20. The computed results are compared to the compressible boundary-layer solutions. The computed flow results are smooth, even through the corner interface points. Freestream errors in the temperature are less than 0.4%, and the error of the temperature along the plate is at most 0.35%.

Corresponding results for the $M = 0.6$ subsonic flow at $\mathrm{Re} = 2500$ are shown in Figs. 21 and 22. In this case all the interface points are subsonic. Superimposed on the velocity vector plot is the computed position of the edge of the boundary layer defined as 99% of the free-stream value. The computed temperature and tangential velocity profiles at the vertical interfaces are compared to the boundary-layer solutions in Fig. 22. Again, we see excellent agreement between the two and the solutions are smooth through the

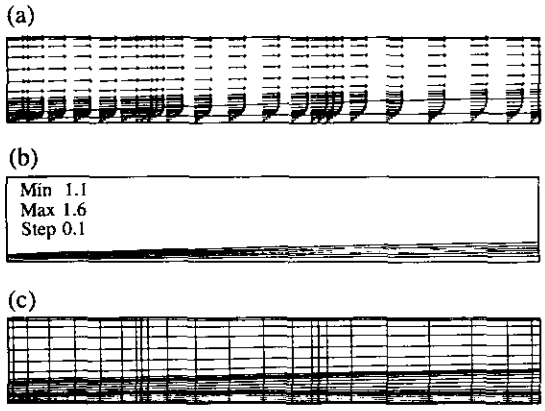

FIG. 19. Velocity vectors (a), temperature contours (b), and grid (c) for the $M = 2$ flow over a flat plate.

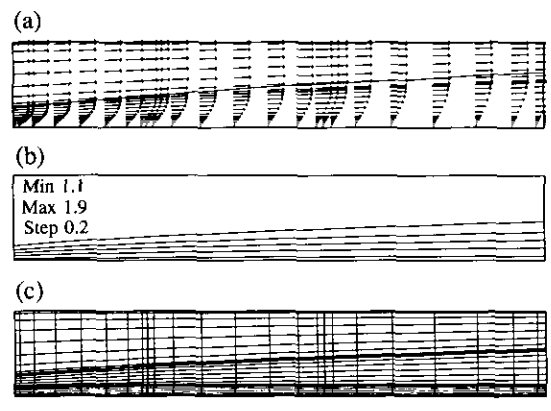

FIG. 21. Velocity vectors (a), temperature contours (b), and grid (c) for the $M = 0.6$ flow over a flat plate.

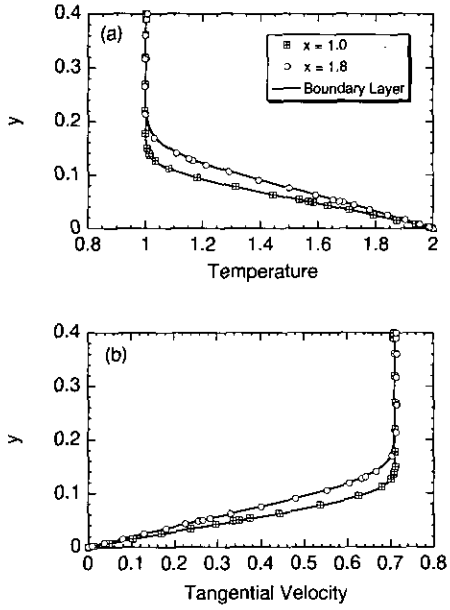

FIG. 22. Temperature (a) and tangential velocity profiles (b) along the vertical interfaces for the $M = 0.6$ boundary layer flow.

interfaces. The freestream errors in the temperature are at most 0.2%.

4.2. Transonic Flow in a Converging–Diverging Nozzle

As a final example, we solve a transonic flow in a two-dimensional converging–diverging nozzle. The nozzle contour that we use comes from an investigation of the velocity flowfields in chemical laser nozzles [21]. Of the models tested in [21], we choose the 5× configuration 1 that has a throat gap of 0.05 in. The flow parameters were a total temperature of 520 °R and Reynolds number of 1200 based on the throat gap. Additionally, we solve for an isothermal wall, set to the stagnation temperature, and a Prandtl number of 0.72.

The nozzle geometry and grid are shown in Fig. 23. We solve for the flow in the upper half of the nozzle and use a symmetry condition along the lower boundary. The throat was placed at $x = 0$, the inlet at $x = -3$ and the exit at $x = 15$, all scaled to the throat gap. Twenty-one subdomains cover the domain, chosen to resolve well the flow in the region of the throat and to resolve the boundary layer, which grows rapidly in the diverging portion of the nozzle.

Boundary conditions were applied as described in the

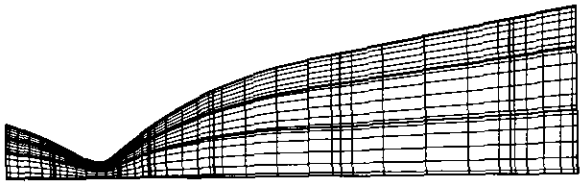

FIG. 23. Nozzle geometry and grid.

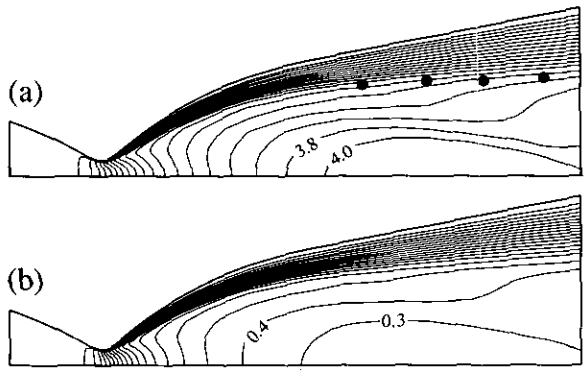

FIG. 24. Solution contours for the nozzle: (a) Mach number; (b) temperature. The black circles mark measured boundary layer positions from [21].

previous section. For the initial and inflow boundary conditions, we use the quasi-one-dimensional inviscid solution. At the inflow, where the flow is subsonic, we used a smoothed crossflow velocity profile. As in [21], we did not see a strong dependence of the downstream flow to the actual shape of the velocity profile. Symmetry conditions $v = 0$, $P_y = u_y = \rho_y = 0$ were applied along the lower boundary.

Solution contours of the Mach number and temperature for the steady solution are shown in Fig. 24. Plotted with the

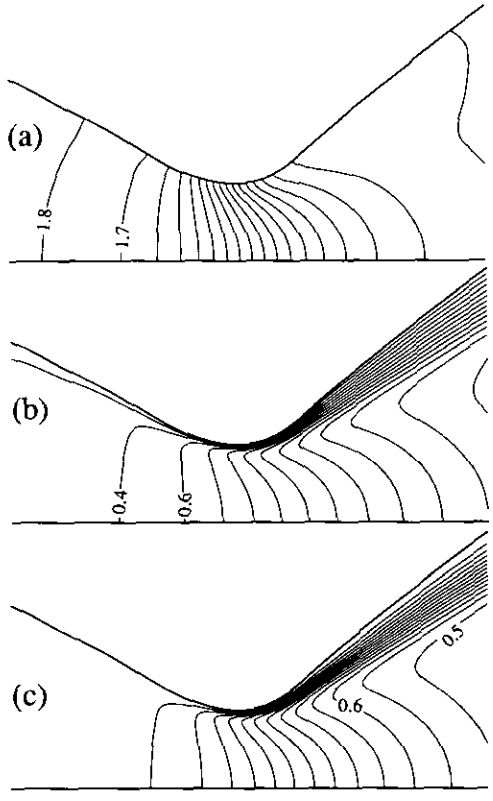

FIG. 25. Expanded view of throat region: (a) Pressure, (b) Mach number, (c) temperature.

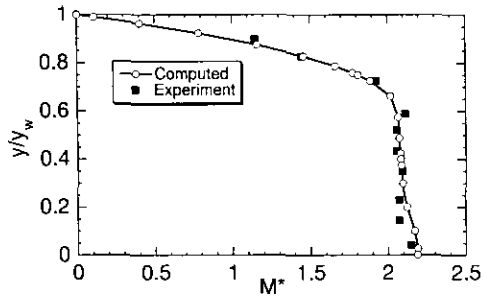

FIG. 26. Velocity scaled to throat sound speed at $x = 13$.

Mach contours are experimentally determined positions of the boundary layer from [21]. Again, the solutions are smooth through the subdomain interfaces. Visible in the essentially inviscid core of the exit is the wave generated at the joint between the curved and straight portions of the wall in the exit portion of the nozzle. The Mach contours are qualitatively similar to the computation made by Cline [22] who used a MacCormack scheme. An expanded view of the throat region that shows the smooth pressure, Mach, and the temperature contours there, is shown in Fig. 25. Finally, Fig. 26 shows the vertical profile of the fluid velocity divided by the sound speed at the throat along the last vertical interface drawn in Fig. 23, which corresponds to $x = 13$. Good agreement is observed between the computed results and the values measured in Ref. [21].

5. SUMMARY

We have developed a multidomain spectral collocation method for solving the non-conservative form of the compressible Navier–Stokes equations. A main advantage of the method over a single domain method is the ability to easily distribute subdomain boundaries and the number of points to resolve features such as boundary layers. The method is designed for nonoverlapping grids. The current limitation is that the approximation must be "conforming," in the sense that the grid lines must be continuous across the interfaces.

At interfaces between subdomains, the advection terms are treated with the characteristic correction method used in [5] for the inviscid Euler equations. In this way, in regions where the viscosity is not important, the method behaves in the same way as it would for an inviscid flow. The diffusion terms are treated with a penalty method that was originally developed for the approximation of the Poisson equation. The penalty, which has a factor that grows as the square of the number of points, is chosen to stabilize the weighted average of the viscous terms computed on opposite sides of the interface. The procedure can be extended naturally to three space dimensions.

Spectral accuracy was demonstrated on linear model problems in one and two space dimensions for which the exact solutions are known. The method was then applied to a subsonic and a supersonic flow over a flat plate. These calculations were compared to solutions of the boundary-layer equations. We saw that the solutions are smooth for interfaces placed in subsonic or supersonic regions of the flow. The final example solved a transonic flow in a converging–diverging nozzle. Again, the solution was stable and smooth through the interfaces. A good comparison (error better than 15%) between the computed and experimental velocity profile at one vertical plane was observed.

ACKNOWLEDGMENTS

The author thanks Drs. C. D. Pruett and C. L. Streett for their compressible boundary layer code and Dr. J. Webb for helpful suggestions. This research was supported in part by the National Aeronautics and Space Administration under NASA Contract NAG1-862 and by the U. S. Department of Energy through Contract DE-FC05-85ER250000.

REFERENCES

1. C. Canuto, M. Y. Hussaini, A. Quarteroni, and T. A. Zang, *Spectral Methods in Fluid Mechanics* (Springer-Verlag, New York, 1987).
2. K. Z. Korczak and A. T. Patera, *J. Comput. Phys.* **62**, 361 (1986).
3. H. C. Ku, T. D. Taylor, and R. S. Hirsch, in *11th International Conference on Numerical Methods in fluid Dynamics*, Lecture Notes in Physics, Vol. 323, edited by D. L. Dwoyer, M. Y. Hussaini, and R. G. Voigt (Springer-Verlag, New York, 1989), p. 349.
4. M. Macaraeg and C. L. Streett, *Int. J. Numer. Methods Fluids* **8**, 1121 (1988).
5. D. A. Kopriva, *J. Comput. Phys.* **96**, 428 (1991).
6. P. Hanley, *J. Comput. Phys.* **108**, 153 (1993).
7. A. Quarteroni, *SIAM J. Sci. Statist. Comput.* **11**, 1029 (1990).
8. D. A. Kopriva, *Comput. and Fluids* **21**, 247 (1992).
9. D. A. Kopriva, *AIAA J.* **31**, 2227 (1993).
10. D. A. Kopriva and M. Y. Hussaini, in *Domain Decomposition Methods*, edited by T. F. Chan, R. Glowinski, J. Periaux, and O. B. Wildlund (SIAM, Philadelphia, 1989), p. 240.
11. D. G. Lasseigne, T. L. Jackson, and M. Y. Hussaini, *Phys. Fluids A* **3**, 1972 (1991).
12. M. Deville and E. Mund, *J. Comput. Phys.* **60**, 517 (1985).
13. Y. Morchoisne, in *Spectral Methods for Partial Differential Equations*, edited by R. G. Voigt, D. Gottlieb, and M. Y. Hussaini (SIAM-CMBS, Philadelphia, 1984), p. 181.
14. D. Funaro, *Numer. Methods Part. Diff. Eqs.* **2**, 187 (1986).
15. D. Funaro, *Numer. Math.* **52**, 329 (1988).
16. Ames Research Staff, NACA Rep 1135, 1958 (unpublished).
17. D. A. Kopriva, *SIAM J. Sci. Statist. Comput.* **10**, 120 (1989).
18. C. Basdevant, M. Deville, P. Haldenwang, J. M. Lacroix, J. Ouazzani, R. Peyret, P. Orlandi, and A. T. Patera, *Comput. and Fluids* **14**, 23 (1986).
19. D. A. Kopriva, *AIAA J.* **31**, 1235 (1993).
20. C. D. Pruett and C. L. Streett, *Int. J. Numer. Methods Fluids* **13**, 713 (1991).
21. J. C. Hyde and G. A. Hosack, AIAA Paper 73-641, July 1973 (unpublished).
22. M. C. Cline, *AIAA J.* **14**, 295 (1976).